Carbon dioxide reforming of methane over promoted $Ni_xMg_{1-x}O$ (1 1 1) platelet catalyst derived from solvothermal synthesis

Mingjue Yu [a], Kake Zhu [a,*], Zhicheng Liu [b], Haipeng Xiao [a], Wei Deng [a], Xinggui Zhou [a]

[a] UNILAB, State Key Lab of Chemical Engineering, School of Chemical Engineering, East China University of Science and Technology, 130 Meilong Road, Shanghai 200237, PR China
[b] Shanghai Research Institute of Petrochemical Technology, 1658 Pudong North Road, Shanghai 201208, PR China

ARTICLE INFO

ABSTRACT

A bottom-up approach is developed to synthesize Sn, Ce, Mn, or Co promoted $Ni_xMg_{1-x}O$ catalysts enclosed by Tasker III type polar (1 1 1) facets. Sn and Co are evenly distributed on $Ni_xMg_{1-x}O$, whereas Ce and Mn segregate as separate oxides. X-ray diffraction (XRD), N_2 physisorpt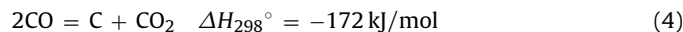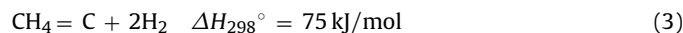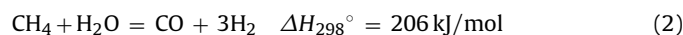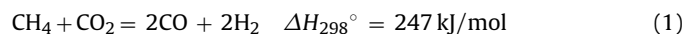ion, X-ray photoelectron spectroscopy (XPS), and Transmission Electron Microscopic (TEM) measurements are carried out to understand the structure/composition of both fresh and spent catalysts. H_2-Temperature Programmed Hydrogenation (TPH), XPS and Thermogravimetric analysis (TG) are employed to elucidate the types of coke formed on the spent catalysts. Mn does not show obvious enhancement to catalytic stability towards C_β formation, and a lower activity is observed as it separates from catalyst surface and causes agglomeration of $Ni_xMg_{1-x}O$(1 1 1) platelets. C_β and whisker carbons are found for Ce-promoted $Ni_xMg_{1-x}O$(1 1 1) catalyst, for Ce segregates as CeO_2. Both Sn and Co are distinguished to enhance the coke-resistant properties of $Ni_xMg_{1-x}O$ catalyst in CH_4-CO_2 dry reforming, as they inhibit the formation of C_β. Activation energy (E_a) measurements show that Sn lowers the activity of Ni surfaces, while Co does not passivate the intrinsic activity of Ni surfaces. Under more critical reaction conditions with CH_4/CO_2 ratio of 3 and diluent gas free, Co is found to enhance the lifespan of $Ni_xMg_{1-x}O$ (1 1 1) catalyst.

© 2013 Elsevier B.V. All rights reserved.
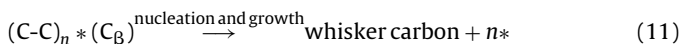
1. Introduction

Dry reforming of methane and carbon dioxide (reaction (1)) gains tremendous research interests as it consumes two major greenhouse gases and alleviates their detrimental effects on global warming. The produced syngas has lower H_2/CO ratio (close to 1) that is more suitable for the subsequent synthesis of oxygenates such as acetic acid, dimethyl ether, oxo-alcohols, etc.[1]. Commercially, syngas is generated by steam reforming of methane (reaction (2)), and a syngas with H_2/CO ratio of 3 is generated. Additional steps are required to adjust the ratio for downstream applications, for instance, methanol synthesis. In practice, to suppress coke deposition on catalyst, a feedstock with H_2O/CH_4 ratio above 1.4 is adopted and hence suffers from energy penalty by heating excessive steam to *ca.* 800 °C [2]. The utility of dry reforming is suitable to convert gas mixtures of CH_4 and CO_2 that are found in natural gas fields at low cost, when separation is no longer needed. To date, CH_4-CO_2 dry reforming has not been commercialized, partly due to the severe coke deposition that is associated with

interruption of continuous manipulation caused by reactor plug, catalyst deactivation, or catalyst pulverization.
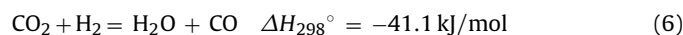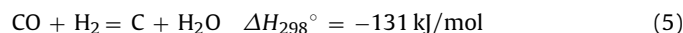
$$CH_4 + CO_2 = 2CO + 2H_2 \quad \Delta H_{298}° = 247 \, kJ/mol \tag{1}$$

$$CH_4 + H_2O = CO + 3H_2 \quad \Delta H_{298}° = 206 \, kJ/mol \tag{2}$$

$$CH_4 = C + 2H_2 \quad \Delta H_{298}° = 75 \, kJ/mol \tag{3}$$

$$2CO = C + CO_2 \quad \Delta H_{298}° = -172 \, kJ/mol \tag{4}$$

$$CO + H_2 = C + H_2O \quad \Delta H_{298}° = -131 \, kJ/mol \tag{5}$$

$$CO_2 + H_2 = H_2O + CO \quad \Delta H_{298}° = -41.1 \, kJ/mol \tag{6}$$

$$CH_4 + * = CH_x\text{-}* + (4-x)/2H_2 \tag{7}$$

$$CH_x\text{-}* = C\text{-}* (C_\alpha) + x/2H_2 \tag{8}$$

$$C\text{-}* + C\text{-}* = (C\text{-}C)_n*(C_\beta) \tag{9}$$

$$C\text{-}* + O* = CO + 2* \tag{10}$$

$$(C-C)_n * (C_\beta) \xrightarrow{\text{nucleation and growth}} \text{whisker carbon} + n* \qquad (11)$$

The optional dry reforming catalysts are categorized into transition- and noble-metal catalysts. Despite the fact that noble metals (Rh, Ru, Pd, and Pt) are more resistant to coke deposition at elevated temperatures, nickel is invariably chosen in industry for the wide availability and related low-cost [3]. The problematic issue that rises up by nickel is its propensity to coke formation at reforming conditions, as a result of strong affinity of carbon to nickel surfaces [4]. Carbon deposition is attributed to three reactions: methane fragmentation (reaction (3)), Boudouard reaction (CO disproportionation, reaction (4)) and CO hydrogenation (reaction (5)). The reaction is also escorted by reverse-water-gas-shift reaction (RWGS, reaction (6)) that affects H_2/CO ratio or contributes to gasification of surface carbonaceous species by steam. Thermodynamically, methane fragmentation is favored at high temperatures, and is hence the main cause of carbon deposition in methane dry reforming [5]. In the course of the reaction, CH_4 is decomposed into CH_{4-x} ($x = 1$–4) and H_2 (reactions (7) and (8)). Deprotonated surface C^* species can accumulate on Ni surfaces as deprotonation rate for CH_4 is lower than these for CH_{4-x}, and further deprotonation is progressively accelerated [6]. When excessive C_α is accumulated by sluggish gasification, C_α is converted into C_β via polymerization [7] (reaction (9)). At low surface coverage, reactive intermediate mono-atomic carbon (C_α) is formed which can be facilely gasified by surface O^* or OH^* species to produce CO (reaction (10)). C_β is recalcitrant towards gasification and can nucleate and grow to mechanically strong carbon whiskers [8] (reaction (11)). Theoretical studies and *in situ* Transmission Electronic Microscopic (TEM) observations have disclosed that whisker carbon nucleates preferentially on step sites of Ni surfaces where they are bound more strongly for the under coordination nature. Moreover, once carbon atoms polymerize at the step sites, they migrate to terrace sites and form a flake of graphene layer whose growth leads to encapsulation of Ni particles [6,9]. More importantly, when the graphene flakes on Ni terraces are smaller than a critical size (<2.5 nm in diameter), the nucleation center is predicted theoretically to be unstable and tends to dissociate and disappear [6]. However, above this critical size, the energy cost caused by periphery carbon atoms is overweighed by the energy gain in the graphene flake center and the growth becomes spontaneous, a phenomenon that is also corroborated by experiments [6,10]. From the aforementioned in depth studies, it has been recognized that small Ni particle size and blockage of carbon nucleation centers (also called ensemble control) are the keys to restrict coke deposition kinetically.

Reduction of Ni^{2+} containing solid solutions or Ni^{2+} isomorphous substituted mixed oxides is realized as an effective way to maintain the Ni particle size small [3,11–13]. NiO and MgO form an ideal solid solution catalyst for CH_4 reforming reactions, but the performances are highly dependent on preparation protocols [13–27]. Hu and Ruckenstein [13–16,20,28,29] have found that $Ni_xMg_{1-x}O$ derived from impregnating specific MgO (from Aldrich) at low loadings (9.2–28.6 wt.%) are durable catalyst for CH_4-CO_2 dry reforming at 790 °C, while little activity was observed for NiO content <4.9 wt.%. Fujimoto et al. [21,30] have observed that $Ni_{0.03}Mg_{0.97}O$ derived from co-precipitation is the optimal composition as robust dry reforming catalyst, albeit at elevated reaction temperature of 850 °C. Xu and co-workers [17,18,31] have found that not all Ni in the solid solution is reduced for impregnated MgO derived from an alcogel method, and the structure is representatively denoted as Ni^0/Ni_xMg_yO, where the unreduced Ni^{2+} has strong interaction with Ni^0 that is important to retain the small size. The promoting effect has been explored for Pt, Pd, Rh, Sn, and Ge. It has been confirmed that these promoters enhance long term stability [22,24,25,32]. In these studies, the introductions of promoters are achieved via impregnation of as-synthesized solid solution, which may not ensure the highly homogeneous distribution of promoters on Ni surfaces.

Spatial distribution of Ni and promoters are equally important to the enhancement of anti-coking property, as the local contents of promoters determine quantitatively the relative activation energy scenario for ensemble control [33–35]. Sporadic zoning of Ni or local absence of promoters can lead to whisker carbon growth and migration of encapsulated Ni particles. One reason for the industrially viable SPARG process is that the gas phase replenish of H_2S to retain the ensemble control is dynamic and homogeneous, ascertaining the coke-resistance and catalytic fate microscopically uniform [36]. As conventional impregnation method for catalyst preparation suffers from uneven spatial distribution of Ni [37], the current challenge is to find ways that can tailor the spatial distribution of both Ni and promoters to enhance the coke-resistance of Ni catalyst. The problems mentioned above signpost us to find new routes that can synthesize solid solution catalyst in a controllable way, which is required to turn the valuable knowledge from surface studies into a practical catalyst.

In preceding articles, we have developed the synthesis methods for NiO [38,39], MgO [40,41], or bimetallic $Ni_xMg_{1-x}O$ [42] platelets enclosed by (1 1 1) facets. It is noteworthy that the (1 1 1) plane of these rocksalt structure is made up of alternating positively charged metal cations and negatively charged oxygen anions, resulting in that a polarity perpendicular to the surface is built up. Such facets are categorized as Tasker III type and feature high surface energy and reactivity [43]. Although $Ni_xMg_{1-x}O$ (1 1 1) platelets are more stable than the same catalyst derived from conventional co-precipitation route [42], the deposition of recalcitrant carbon cannot be completely inhibited without promoters (see below). In the current work, we explore the introduction of promoter metals such as Sn, Ce, Mn, Co into the intermediate to form a M-Ni_xMg_{1-x} (OH)(OCH$_3$) platelet, as a means to tailor elemental spatial distribution of both Ni and promoters. The catalytic performances and structural evolution of M-$Ni_xMg_{1-x}O$ catalysts and types of deposited coke are also investigated. It is indeed found that only evenly distributed promoters such as Sn and Co can inhibit C_β deposition. Co is preferred for the non-passivation of catalyst activity and coke-resistance under harsh reaction conditions.

2. Experimental

2.1. Catalysts preparation

Magnesium acetate tetrahydrate, cobalt(II) acetate tetrahydrate, Mn(II) acetate tetrahydrate, Sn(II) acetate, and methanol were purchased from Sinopharm Chemical Reagent Co. Ltd. Cerium(III) acetate was provided by Shanghai Diyang Chemical Company. All chemicals are employed directly for the synthesis of catalyst without further purifications. In a typical synthesis, Ni, Mg and Sn acetates with molar composition of 0.10:0.90:0.01 were dissolved in methanol to form a homogeneous clear solution of 0.1 M (total metallic basis). The mixture was stirred continuously for 5 h before being charged into a 200 ml Telfon-lined stainless steel autoclave and heated for 48 h at 180 °C. The solid educts were recovered by filtration and washed by copious amount (3 times, total 100 ml) of methanol. The powder was dried in an oven at 60 °C for 12 h before heated in a muffle oven to 800 °C via a ramp of 2 °C/min in air, and soaked for 6 h. Part of the intermediate educts was collected and subject to structural characterizations to validate the preparation method. Other samples were prepared in the same way, in the case of a promoter-free sample, no promoter precursor was introduced. The as-synthesized ultrafine powder is labeled M$_{0.01}$-Ni$_{0.10}$Mg$_{0.90}$(OH)(OCH$_3$) (M = Co, Mn, Ce, Sn), and the

corresponding mixed oxide after calcination is denoted as $M_{0.01}$-$Ni_{0.10}Mg_{0.90}O$.

2.2. Characterization techniques

Powder X-ray diffraction (XRD) patterns were recorded on a Rigaku D/Max-RC powder diffractometer using Cu Kα radiation (operated at 40 kV and 100 mA, λ = 1.54178 Å). The diffractograms were collected in the 2θ range of 10–80° with a 2θ step size of 0.01° and a step time of 10 s. Scanning Electronic Microscopic (SEM) images of the as-synthesized intermediates were taken on a JEOL JSM-6700F Field Emission SEM setup. TEM images of the powder samples were recorded on a HITACHI H-800 instrument operated at 200 kV. The samples were prepared via dispersing in ethanol on 400 mesh copper grids pre-coated with thin carbon films. Specific surface areas were deduced from N_2 physisorption using the standard Brunauer–Emmett–Teller (BET) model. Before measurements, all samples were subject to degassing at 350 °C overnight under vacuum. H_2-temperature programmed reduction (H_2-TPR) of samples (100 mg) placed at the bottom of the U-shaped quartz tube was investigated by heating samples in H_2 (5 vol.%)/Ar flow (30 ml/min) at a heating rate of 10 °C/min from 20 to 850 °C, and soaked at 850 °C for 30 min till no H_2 consumption was observed. The H_2 consumption was monitored by thermo-conductivity detector (TCD). The amount of H_2 consumption was calibrated by Ag_2O titration, assuming Ag in Ag_2O was completely reduced to Ag^0. H_2-TPH patterns ranging from 25 to 850 °C to the spent catalysts were obtained by the same ramp and flow rate. X-ray Photoelectron spectra (XPS) analyses were performed on a Thermo Fisher Scientific ESCALAB 250Xi spectrometer, using Al-Kα radiation (1486.6 eV, pass energy 20.0 eV). The base pressure of the instrument is 1×10^{-8} to 1×10^{-9} Torr. The background contribution B(E) (obtained by Shirley method) caused by inelastic process was subtracted, whereas the curve-fitting was performed with Gaussian–Lorentzian profile by the standard XPS PEAK 4.1 software. The binding energies (BEs) over supported catalysts were calibrated using C1s peak at 284.8 eV. XPS spectra were recorded at $\theta = 90°$ of X-ray sources. Thermal gravimetric analyses (TGA) were performed on a thermo-gravimetric analyzer (SDT-Q 600) instruments under air to estimate the thermal decomposition of intermediate $M_{0.01}$-$Ni_{0.10}Mg_{0.90}(OH)(OCH_3)$. The samples were heated in air flow at a heating rate of 10 °C/min to 850 °C, with the flow rate kept at 50 ml/min. Similar procedures were also adopted to determine the deposited coke amount for the spent catalysts. Infrared (IR) studies were recorded by a FT-IR THERMO NICOLET 6700 NEXUS spectrophotometer. The scanning area is 4000–400 cm^{-1}. The spectrum resolution was 4 cm^{-1} and 32 scans were collected.

2.3. Catalytic assessments

The evaluation of catalysts was conducted in a fixed-bed reactor made of quartz tube, whose i.d. was 10 mm. 200 mg catalyst was pressed into pellets and sieved to 40–60 mesh. The catalyst was mounted in the tubular reactor made from quartz and diluted with quartz sand, mounted with quartz wool. A capillary quartz tube (i.d. 1.5 mm) was inserted, from the exit side of the reactor, into the catalyst bed to introduce a thermal couple, which permits a measurement of the temperature at the catalyst bed. Before the measurements, a standard gas mixture provided by Shanghai Institute of Quality Inspection and Technical Research was employed to calibrate the gas chromatography (GC) system. Based on literature, mass transfer was mostly eliminated as such conditions of high flow rate and small amount of catalyst with small particle sizes [5,44]. Prior to catalytic test, a blank test was carried out and no activity was detected without catalyst. The feeding gas flow rate to the reactor was set at 68 ml/min, with a gas molar
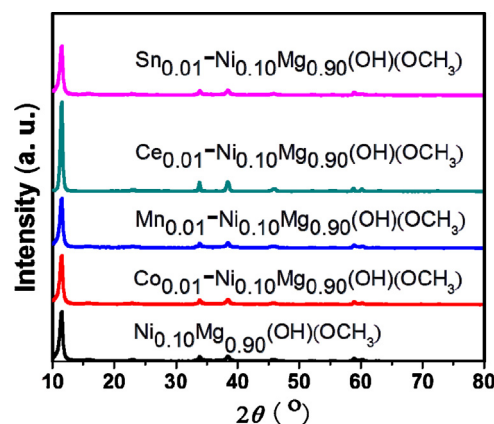

Fig. 1. XRD patterns of as-synthesized intermediates $M_{0.01}$-$Ni_{0.10}Mg_{0.90}(OH)(OCH_3)$.

ratio $CH_4:CO_2:N_2 = 25:25:18$ or $CH_4:CO_2 = 51:17$, under normal and harsh reaction conditions, respectively. The flow rate (Gas Hour Space Velocity, GHSV) of the feed was 20,000 ml h^{-1} g^{-1} cat. The mounted catalyst was subjected to *in situ* reduction under H_2 atmosphere at a flow rate of 60 ml/min at 800 °C for 2 h before catalytic test. The effluent gas was separated and determined by GC-9860 (Shanghai Qi Yang Instrument), equipped with a TDX-01 column and an on-line TCD. CH_4, CO_2 conversions, selectivity to H_2 and CO, H_2/CO ratio are defined as follows:

$$X_{CH_4} = \frac{F_{CH_4,in} - F_{CH_4,out}}{F_{CH_4,in}}, \quad X_{CO_2} = \frac{F_{CO_2,in} - F_{CO_2,out}}{F_{CO_2,in}}, \quad S_{H_2}$$

$$= \frac{F_{H_2,out}}{2\left(F_{CH_4,in} - F_{CH_4,out}\right)}, \quad S_{CO}$$

$$= \frac{F_{CO,out}}{\left(F_{CH_4,in} - F_{CH_4,out}\right) + \left(F_{CO_2,in} - F_{CO_2,out}\right)}, \quad H_2/CO = \frac{S_{H_2}}{S_{CO}}.$$

Kinetic studies were performed under identical conditions previously employed by Wei and Iglesia [44], to preclude the effect of diffusion to the measurement of activation energies. For each measurement, 30 mg catalyst (40–60 mesh) diluted by γ-Al_2O_3 powders was mixed with 500 mg quartz sand of the same size, and then mounted into the reactor to reach a differential condition, and the conversion for CH_4 was controlled below 5%. Appropriate criteria were employed to ensure the validity of the measurements. From previous reports, it has been established that on $Ni_xMg_{1-x}O$ the reaction rate is first order of P_{CH_4}, and can be expressed as $r = kP_{CH_4}$ [10,44]. Activation energy is derived by using this rate expression and the standard Arrhenius plot.

3. Results and discussion

3.1. Catalyst precursor preparation and characterizations

The structures of the intermediate $M_{0.01}$-$Ni_{0.10}Mg_{0.90}(OH)(OCH_3)$ educts are characterized by XRD, SEM, and TEM. Fig. 1 shows the XRD patterns, which have not been previously known, and are identical to the magnesium or nickel analogues, $Mg(OH)_{1.3}(OCH_3)_{0.7}$ (JCPDS file No. 22-1788), $Ni[(OH)_{2/3}(OCH_3)_{1/3}]_2$ or bimetallic $Ni_xMg_{1-x}(OH)(OCH_3)$ [38,41,42,45,46], but with slightly different lattice parameters. These patterns can be indexed to a phase pure *R-3m* (space group No. 166, $a = 0.313$–0.307 nm, $c = 2.29$–2.39 nm) structure (Supporting information, Table S1). The characteristic diffraction for (0 0 3) is unique for the high intensity of peaks for $l = 3n$, implying a strong anisotropic nature of the intermediate compound
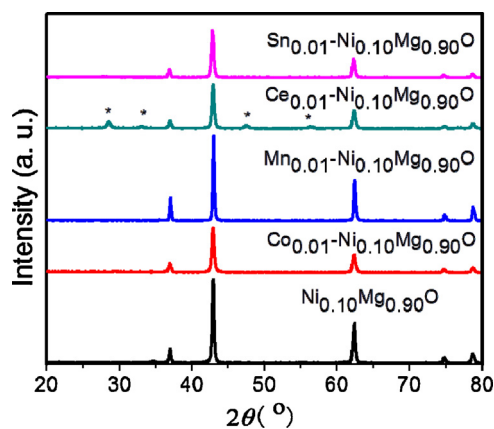
Fig. 2. XRD patterns for pristine and promoted $Ni_{0.10}Mg_{0.90}O$ solid solutions.

with respect to crystalline orientation along *c* axis. These results indicate that the introduction of promoter elements into the $M_{0.01}$-$Ni_{0.10}Mg_{0.90}(OH)(OCH_3)$ intermediate by the present method does not destroy the integrity of the bulk structure or cause segregation of a separate phase. SEM measurements reveal that the samples are unanimously made up of platelet-shaped nanoparticles of several microns with a thickness of *ca.* 50 nm (Fig. S1). No obvious difference in morphology can be distinguished for samples except $Mn_{0.01}$-$Ni_{0.10}Mg_{0.90}(OH)(OCH_3)$, which appears as stacked platelets instead of isolated ones. TEM is employed to unravel the microscopic structure. Representative TEM images show that the platelets lay on the copper grid are perpendicular to the platelet surface (Fig. S2). ED patterns show that the surface is along [0 0 1] axis of an *R-3m* structure, and is in line with XRD observations. For all the platelets observed, the surfaces are found to be perpendicular to [0 0 1] axis, which is typical for the monometallic counterparts [38–41,45,46]. The corresponding IR and TG patterns are displayed in Figs. S3 and S4, respectively, and are close to the nickel/magnesium analogues [38–42]. From these characterizations, it is concluded that the selected promoters can be introduced into the structure of these intermediates.

3.2. Characterization of fresh catalysts

After combustive decomposition, powder form oxides are produced. The XRD patterns of these oxides are displayed in Fig. 2. The thermal decompositions of intermediates produce $Ni_{0.10}Mg_{0.90}O$ in all the samples, as rocksalt structured solid solutions are observed in all samples, with a structure matches NiO (JCPDS card No. 78-0643, space group: *Fm-3m*) or periclase MgO (JCPDS file No. 87-0653). No other phases can be found for promoters except in $Ce_{0.01}$-$Ni_{0.10}Mg_{0.90}O$, in which a clear fluorite phase attributable to CeO_2 (JCPDS Card No. 34-0394) is observed. As MgO and CeO_2 are nearly immiscible, no ternary compound exists in the system [47]. From typical TEM images (Figs. S5–S8), it is also detected that the platelet-like morphology is inherited from the intermediates, because the thermolysis of $M_{0.01}$-$Ni_{0.10}Mg_{0.90}(OH)(OCH_3)$ is a topotactic transformation, the same as for the monometallic counterparts [38,41,42,46]. A careful ED measurement shows that the (1 1 1) surface of rocksalt structure is normal to the platelet. In the thermolysis process, a (0 0 1) facets enclosed *R-3m* structure is transformed into a rocksalt oxides covered by Tasker (III) type (1 1 1) planes. The morphology is completely different from the $Ni_{0.03}Mg_{0.97}O$ derived from co-precipitation by Fujimoto et al. [22], who have observed a typical cube-like morphology. The exposing surfaces in their catalysts are not determined, but it is very likely to be the most stable (1 0 0) facets of typical rocksalt structure (Tasker I type) [22]. The oxide platelets are porous, because the thermal
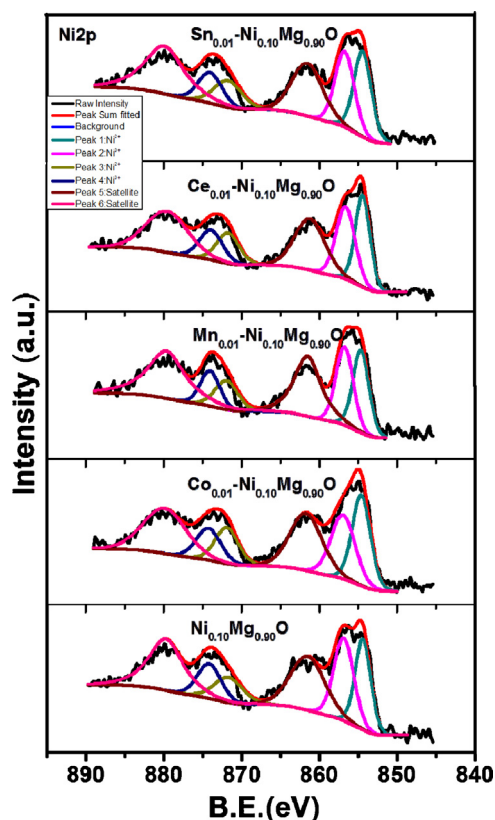

Fig. 3. Ni 2p XPS patterns of fresh $M_{0.01}$-$Ni_{0.10}Mg_{0.90}O$.

decomposition causes lattice shrinkage and porosity is left after release of organics. Elemental mapping of $Sn_{0.01}$-$Ni_{0.10}Mg_{0.90}O$ discloses that all elements are homogeneously distributed over the sample (Fig. S5), implying that most Sn is homogeneously distributed on $Ni_{0.10}Mg_{0.90}O$. Ce, on the other hand, segregates as tiny particulates (Fig. S6), coinciding with XRD observation that crystalline CeO_2 coexists with $Ni_{0.10}Mg_{0.90}O$ solid solution (Fig. 2). CeO_2 normally possesses a coordinate number of 8 in fluorite structure, whereas in a rocksalt structure the coordinate number is 6, and such a discrepancy after calcinations causes the segregation of CeO_2 phase [47]. From the elemental mapping measurement for $Mn_{0.01}$-$Ni_{0.10}Mg_{0.90}O$ (Fig. S7), it is also found that Mn presents as segregated moieties upon calcinations, despite that no crystalline phase is found by XRD measurement (Fig. 2). In the case of $Co_{0.01}$-$Ni_{0.10}Mg_{0.90}O$ (Fig. S8), Co is detected to be evenly distributed in $Ni_{0.10}Mg_{0.90}O$. The incorporation of Sn or Co is possible because their atomic radii are close to Mg^{2+} or Ni^{2+}, and the precursors have a valence number of +2 to form solid solutions with MgO [48,49]. Compositions of the calcined samples are also measured via ICP–AES, and the contents of Ni and promoters are close to the starting materials, as shown in Table 1. The surface areas vary with respect to promoter introduction (Table S2), only Ce-promoted sample exhibits substantial increase in surface area, possibly due to the segregation effect of tiny CeO_2 particulates that stop further agglomeration of high surface energy $Ni_{0.10}Mg_{0.90}O$ (1 1 1) platelets.

XPS is also conducted to gain more detailed information on Ni chemical states in the solid solution, with the profiles for Ni 2p displayed in Fig. 3 and Table S3. A main envelop ranging from 852.5 to 858.0 eV can be discerned. The spectrum can roughly be divided into two edges by spin-orbit coupling, referred to as $2p_{1/2}$ ($\approx$870–885 eV) and $2p_{3/2}$ ($\approx$850–869 eV), respectively. The binding energies for Ni^{2+} and Ni^{3+} appear at *ca.* 854.8 eV and

Table 1
Composition and surface area of fresh $M_{0.01}$-$Ni_{0.10}Mg_{0.90}O$.

Sample	Ni/Mg[a]	M/Ni[a]	Surface composition[b] (mol.%)				
			Ni	C	Mg	O	Promoter
$Ni_{0.10}Mg_{0.90}O$	0.141		3.58	16.90	31.51	48.01	
$Co_{0.01}$-$Ni_{0.10}Mg_{0.90}O$	0.133	0.013	3.44	11.31	38.73	46.01	0.51
$Mn_{0.01}$-$Ni_{0.10}Mg_{0.90}O$	0.124	0.010	3.51	20.00	26.46	47.55	2.47
$Ce_{0.01}$-$Ni_{0.10}Mg_{0.90}O$	0.132	0.008	3.71	17.20	27.40	51.11	0.58
$Sn_{0.01}$-$Ni_{0.10}Mg_{0.90}O$	0.138	0.008	3.35	16.44	31.72	47.03	1.46

[a] Measured by ICP–AES for the bulk composition.
[b] Surface composition measured by XPS.

856.7 eV, respectively [50]. The broad satellite feature centered around 861 eV is attributed to the unscreened $\underline{c}3d^8$ or screened $\underline{c}d^{10}L^2$ final states configuration [50,51]. The shoulder at 856.1 eV due to multiplet splitting of main line at the effect of neighboring NiO is negligible when $x < 0.5$ for $Ni_xMg_{1-x}O$, we therefore rule out this contribution [52]. We assign these two binding energies to the presence of surface Ni^{2+}/Ni^{3+} species, as whose intensity decreased for the spent catalysts (see Section 3.4). As XPS is a surface sensitive technique, the composition measured via XPS reflects a surface composition. Surface Ni^{2+} can be oxidized to Ni^{3+} during calcinations. The spectra for promoted $M_{0.01}$-$Ni_{0.10}Mg_{0.90}O$ are very close to the pristine $Ni_{0.10}Mg_{0.90}O$, indicating Ni is embedded mainly in the MgO matrix and the introduction of promoters does not affect the chemical environment. From XPS spectra for promoters (Fig. S9, Table S4), one can see that Sn $3d_{5/2}$ and Sn $3d_{3/2}$ are at 485.8 and 494.3 eV, respectively, indicating the dominate presence of Sn^{2+} in the fresh catalyst [53]. In addition, some of Sn^{4+} species can also be discerned, which may originate from surface or subsurface Sn^{2+} that has been oxidized during calcinations. As Sn^{4+} can not exist in the rocksalt lattice, such an oxidation leads to surface enrichment of Sn^{4+}, as indicated by its high surface concentration (Table 1). One therefore concludes that the majority of Sn exists as Sn^{2+} in the bulk because only Sn^{2+} can form substituted solid solution with $Ni_{0.10}Mg_{0.90}O$, as implied by XRD (Fig. 2) and elemental mapping results (Fig. S5). Mn $2p_{3/2}$ at 642.5 eV is due to MnO, suggesting the presence of Mn^{2+} [54]. XPS spectra for Co 2p peaks are broadened by multiplet splitting and the two +2 and +3 valence states are not a clear diagnostic feature (780.5 eV, CoO), but the satellite with marked intensity at 5.4 eV strongly suggests that Co^{2+} predominates in the fresh catalyst [55]. This observation is consistent with XRD (Fig. 2) and elemental mapping results (Fig. S8). From the corresponding surface composition measurements derived from XPS data (Table 1), it is also seen that Co content remains close to the bulk composition, strongly indicating that most Co is incorporated into the solid solution.

H_2-TPR has been employed to measure the reducibility of $M_{0.01}$-$Ni_{0.10}Mg_{0.90}O$ solid solutions, which has been recognized as a technique to discriminate various species in solid solutions [17,56,57]. H_2-TPR patterns are depicted in Fig. 4 and Table S5. The profiles for H_2-TPR are continuous and have a broad range of reduction patterns, showing more than one species are reduced for each sample. By rough estimations assuming H_2:Ni = 1, one can expect the degree of reduction normalized to Ni^{2+} is low for pristine $Ni_{0.10}Mg_{0.90}O$, mostly within 50%. The rather weak low temperature reduction peak at 200–270 °C associated with Ni^{3+} surface species locate at surface sites for $Ni_{0.10}Mg_{0.90}O$, but the contribution from surface oxygen anions associated with (1 1 1) facets can not be ruled out [17,42,56]. Besides, a broad peak centered at 460 °C and a shoulder peak ranging from 590 to 750 °C for $Ni_{0.10}Mg_{0.90}O$ owing to outermost and sublayer Ni^{2+} reduction is distinguishable [17], respectively, demonstrating that Ni^{2+} is incorporated into solid solutions and no peaks from isolated NiO is found [17,56]. Above 750 °C, the very broad shoulder peak is ascribed to

the reduction of lattice Ni^{2+} [17,56]. Introduction of Co and Ce does not affect the reduction of Ni^{3+} or surface oxygen associated with (1 1 1) facets that appear at *ca.* 210 °C, as $Ni_{0.10}Mg_{0.90}O$ surfaces are not covered. The absence of these peaks for Mn and Sn contained samples suggests that the surfaces are covered by the promoters, and is consistent with surface composition measurements by XPS (Table 1). Generally, by introducing doped metals, a shift to higher temperatures is observed for the reduction of surface Ni^{2+}, implying strong interaction between surface Ni^{2+} and promoters. The reduction peak at 460 °C observed for pristine $Ni_{0.10}Mg_{0.90}O$ shifts to 560 and 570 °C, for Co- and Sn-promoted samples, respectively. The shift is obviously the result of their stronger affinity to oxygen with respect to Ni, as H_2-TPR reflects the ability to deprive oxygen that produces the corresponding metallic species. A relatively larger H_2 consumption is seen for $Sn_{0.01}$-$Ni_{0.10}Mg_{0.90}O$, possibly due to the simultaneous reduction of surface Sn^{2+}/Sn^{4+} to Sn^0 and Ni^{2+} to Ni^0, as indicated by the highly asymmetric profile of the peak at 570 °C. The effect of Sn is observable because its surface concentration is higher than the bulk and the reduction is hence perceivable. No characteristic TPR peaks ascribable to $MgCo_2O_4$ can be identified for $Co_{0.01}$-$Ni_{0.10}Mg_{0.90}O$, indicating that Co presents in the solid solution as (Co, Ni, Mg)O [58]. For $Mn_{0.01}$-$Ni_{0.10}Mg_{0.90}O$, it is also obvious that the reduction of lattice Ni^{2+} is shifted to 490 °C, possibly due to the coverage of MnO on the $Ni_{0.10}Mg_{0.90}O$ surfaces, and the weak MnO-$Ni_{0.10}Mg_{0.90}O$ interaction is expected
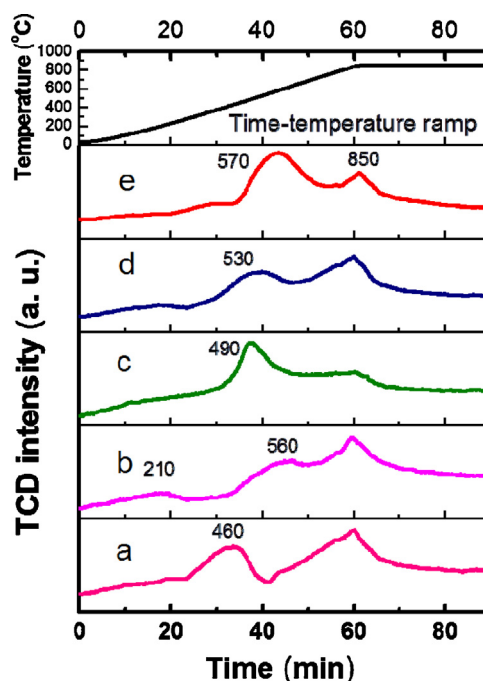
Fig. 4. H_2-TPR profile of (a) $Ni_{0.10}Mg_{0.90}O$, (b) $Co_{0.01}$-$Ni_{0.10}Mg_{0.90}O$, (c) $Mn_{0.01}$-$Ni_{0.10}Mg_{0.90}O$, (d) $Ce_{0.01}$-$Ni_{0.10}Mg_{0.90}O$ and (e) $Sn_{0.01}$-$Ni_{0.10}Mg_{0.90}O$.
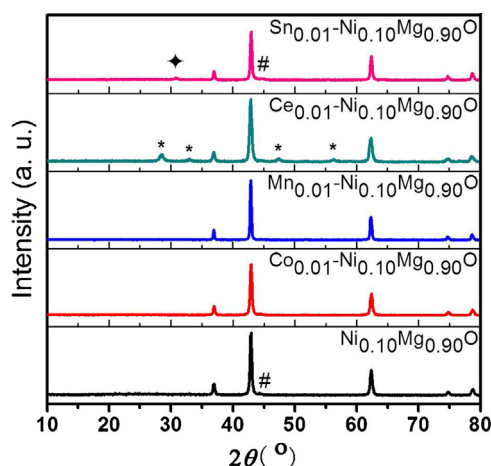
Fig. 5. XRD patterns for as-reduced catalysts. The asterisk, star, and pound signs indicate CeO_2, SnO and Ni^0, respectively.

as the shift is not significant. TPR pattern for $Mn_{0.01}$-$Ni_{0.10}Mg_{0.90}O$ does not show the reduction of Mn_2O_3 or Mn_3O_4, despite the high surface concentration, suggesting that Mn presents as Mn^{2+} in the solid solution that is resistant to further reduction [59]. This is also advocated by XPS detection that suggests the dominant presence of Mn^{2+} (Fig. S9). A perceivable broad peak centered at 530 °C is found in the $Ce_{0.01}$-$Ni_{0.10}Mg_{0.90}O$ sample. The asymmetric nature of the peak indicates that it consists of reduction of $Ni_{0.10}Mg_{0.90}O$ at 460 °C and CeO_2 at *ca.* 530 °C, respectively [60]. This is in line with the fact that CeO_2 presents as isolated CeO_2 nanoparticles on the $Ni_{0.10}Mg_{0.90}O$ surface, and the overall reduction degree for Ni^{2+} is low enough (55%) to permit the reduction of CeO_2 to be observed. From XPS and H_2-TPR measurements, it is seen that Ni exists as either surface species or resides in the solid solution, and most of the reducible species are surface ones. Doping of Sn or Co is homogeneous and leads to stronger oxygen affinity and resistance towards H_2 reduction.

The H_2 reduced samples are also characterized by XRD and TEM techniques. Fig. 5 illustrates the XRD patterns for the reduced samples, a weak diffraction peak at 44.6° can be indexed to face-centered cubic (fcc) Ni (JCPDS card No. 04-0850) (1 1 1) diffraction can be found for samples except Mn- and Co-promoted ones. The lacking of other low intensity diffraction lines for Ni^0 shows that the crystallinity is low for the as-reduced samples. For Sn-promoted sample, another weak diffraction at *ca.* 30.8° can also be identified, which is tentatively ascribed to (0 0 1) diffraction from SnO (JCPDS card No. 24-1342). The TEM measurements reveal that the $Mn_{0.01}$-$Ni_{0.10}Mg_{0.90}O$ has almost identical morphology as the calcined sample, and no distinct Ni particle can be found, strongly indicate that the size of reduced Ni^0 is too small to be discerned by TEM. Besides, the platelet size is the same as the calcined sample. The evidence is consistent with XRD patterns that no Ni^0 diffraction can be identified, showing Mn has a strong influence to the reduction process and can inhibit the growth of Ni^0 particle. For the rest samples, distinct particles are found in TEM measurement, and a particle size distribution can be inferred, as shown in Fig. S10. The absence of diffraction for Ni^0 to $Co_{0.01}$-$Ni_{0.10}Mg_{0.90}O$ can be attributed to the ultra small size of metal particles and the fact that Co-Ni can form alloy easily, which result in broadening of peaks into the baselines. The surface areas for the reduced samples are found to be larger than the calcined ones (Table S2), presumably because that the reduction of Ni^{2+} to Ni^0 leads to corrugated surfaces on the support (Fig. 6).

3.3. Catalytic tests under normal conditions

Catalytic tests are carried out after *in situ* reduction and the performances in dry reforming of CH_4-CO_2 are delineated in Fig. 7. The effect of reaction temperature is unraveled in Fig. 7a–c. For the pristine $Ni_{0.10}Mg_{0.90}O$ catalyst, CH_4 conversion is observed above 500 °C, a temperature required by thermodynamics (Fig. 4 of ref. [11]). The addition of metals such as Sn or Mn reduces the catalytic activities at all temperature range as a result of surface blockage (Table 1) and passivation. This is in line with previous observation that Mn or Sn promotes the long term stability of Ni based catalysts at the cost of Ni surface passivation [61,62]. It is also seen that the H_2/CO ratio is altered with the addition of promoters. RWGS and steam reforming can alter the H_2/CO ratio, as suggested recently [63]. At low CH_4 conversions, CO_2 concentration is relatively high and can lead to increased H_2 conversion to CO and H_2O with respect to reaction (6). We also conducted a 100 h time-on-stream test, with the results demonstrated in Fig. 7d–f. The pristine $Ni_{0.10}Mg_{0.90}O$ is found to be a stable system in terms of activity, and Co, Ce is found to have little impact on the initial activity. $Co_{0.01}$-$Ni_{0.10}Mg_{0.90}O$ exhibits a small enhancement in activity and stability. As coking does not always cause deactivation, the deposition of coke is not obviously reflected by activity variation in $Ni_{0.10}Mg_{0.90}O$ system. Addition of Sn or Mn causes substantial initial activity drop, for $Sn_{0.01}$-$Ni_{0.10}Mg_{0.90}O$, the activity increases with time-on-stream in the first 40 h, then stabilities at this level during the rest of the test. H_2/CO ratio stabilizes as the conversions of reactants become stable. The increase of catalytic activities is assumed to be a result of surface restructuring or further Ni^{2+} reduction under reducing atmosphere, the surface structures of spent catalysts are thereby important. A slow and continuous deactivation is observed for $Mn_{0.01}$-$Ni_{0.10}Mg_{0.90}O$, however, and the catalyst is not stable during the 100 h test. In general, active sites on Ni surfaces are classified into terraces and under-coordinated steps, the former posses a relatively higher activation energy whereas the latter have a lower activation energy. To pristine $Ni_{0.10}Mg_{0.90}O$, the overall activity is reflected by the step sites as the contribution dominates as a result of lower activation energy. When promoters such as Mn or Sn cover these step sites via preferential adsorption, obvious reduction of activity is observed, similar trends are exhibited by lifetime promoters such as Au [34], Ag [64], or S [36]. Co does not passivate the Ni surface, because it is also active for CH_4 reforming reactions, and Co alloys with Ni that promotes the activity of pristine Ni, as proposed by recent theoretical predications [65,66]. CeO_2 segregates in our $Ce_{0.01}$-$Ni_{0.10}Mg_{0.90}O$ case, and does not seem to affect the activity as a result of phase separation.

3.4. Characterizations of spent catalysts and deposited coke

The spent catalysts are characterized by several techniques to understand their structural change during the 100 h catalytic tests. Fig. 8 shows the XRD patterns, it is seen that only CeO_2 presents as segregated oxide in the spent catalyst, which is the same as that of the fresh catalyst (Figs. 2–5). In all samples except $Mn_{0.01}$-$Ni_{0.10}Mg_{0.90}O$, diffractions of (1 1 1) or (2 0 0) from *fcc* structured metallic Ni (JCPDS No. 04-0850) can be resolved at 44.5° and 51.8°, respectively, evidencing that NiO has been partly reduced during the pretreatment and reaction period. Intriguingly, no Ni^0 peaks is seen for $Mn_{0.01}$-$Ni_{0.10}Mg_{0.90}O$, showing that Mn^{2+} strongly inhibits the reduction of surface Ni in $Ni_{0.10}Mg_{0.90}O$ and Ni^0 presents as tiny moieties that is beyond the detection limit of XRD. The resistance towards reduction is in accordance with H_2-TPR results. No peaks from metallic promoters can be detected by XRD, demonstrating these promoters did not grow into particles due to ripening during reaction. No obvious diffractions from whisker carbon are
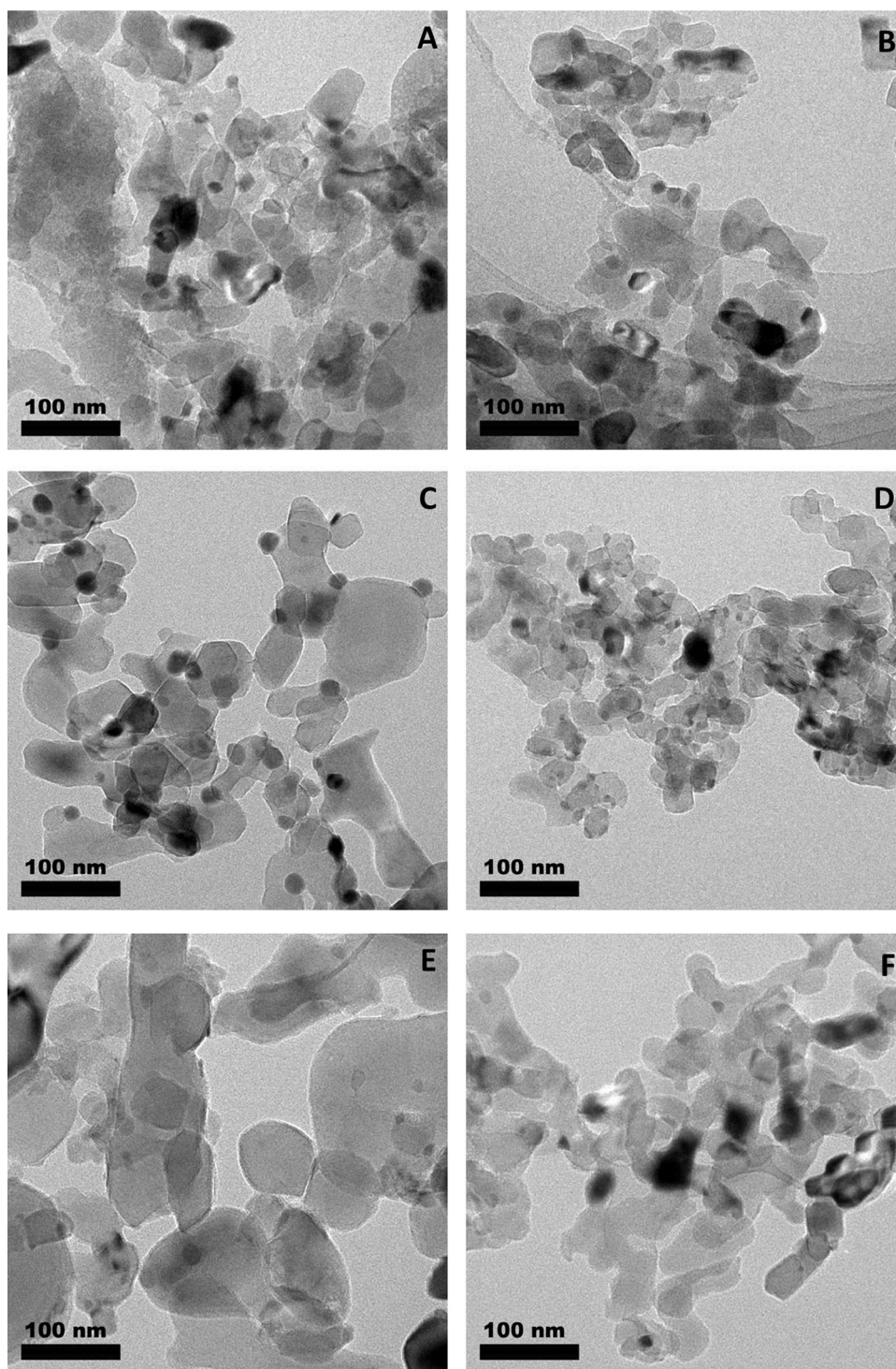
Fig. 6. TEM images of as-reduced $Ni_{0.10}Mg_{0.90}O$ (A, B), $Sn_{0.01}$-$Ni_{0.10}Mg_{0.90}O$ (C), $Ce_{0.01}$-$Ni_{0.10}Mg_{0.90}O$ (D), $Mn_{0.01}$-$Ni_{0.10}Mg_{0.90}O$ (E), and $Co_{0.01}$-$Ni_{0.10}Mg_{0.90}O$ (F).

detected, confirming that the amount of carbon deposited is low and amorphous.

XPS measurements to the spent catalysts composition are shown in Table 2 and Fig. 9. Virtually no Mn is detected in the spent $Mn_{0.01}$-$Ni_{0.10}Mg_{0.90}O$, which is tentatively ascribed to the restructuring of $Mn_{0.01}$-$Ni_{0.10}Mg_{0.90}O$ during catalytic test. Sn is found to be enriched in the surface after 100 h time-on-stream test, due to the reduction of SnO to Sn. Co or Ce does not exhibit substantial surface concentration change after reaction. From the Ni $2P_{3/2}$ XPS spectra of spent catalysts (Fig. 9 and Table S6), one major

peak with binding energy of 855.5–856.5 eV and a small shoulder at 872.8–873.8 eV can be distinguished, which are attributed to Ni^{2+} $2p_{3/2}$ and $2p_{1/2}$, respectively [51]. Besides, satellite peaks at *ca.* 880.0 eV can also be identified. Only a small peak from metallic Ni^0 ($\sim$852.7 eV, $2P_{3/2}$) can be detected, because the outermost layer may has been oxidized by air or moisture during post reaction handling [50,67]. Ni surfaces can be enclosed by carbonaceous species that reduce the surface concentration. Peak intensity of Ni^0 for $Mn_{0.01}$-$Ni_{0.10}Mg_{0.90}O$ catalyst is virtually zero, implying more surface Ni^0 species are covered by carbonaceous species.
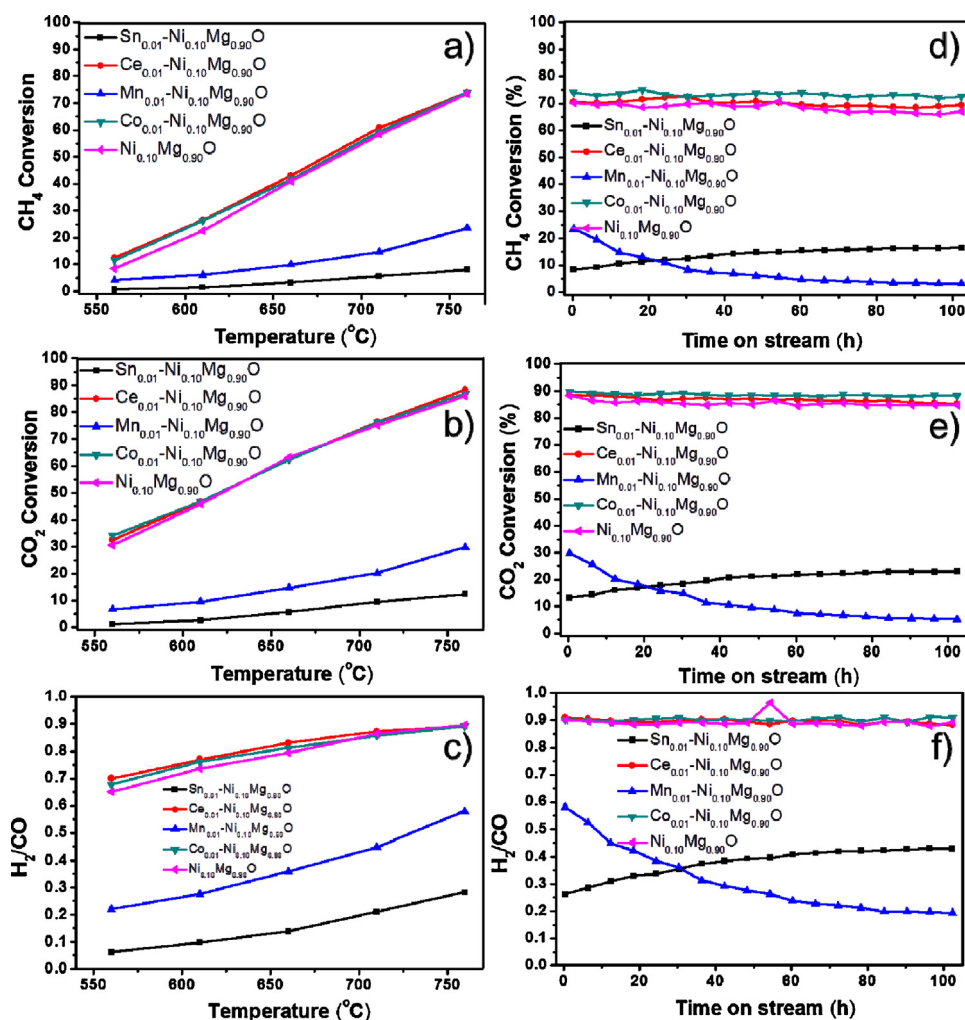
Fig. 7. Temperature-dependent (a–c) and Time-on-stream (d–f) of CH$_4$-CO$_2$ dry reforming performance for pristine and promoted Ni$_{0.10}$Mg$_{0.90}$O in the 100 h test at 760 °C.

H$_2$-Temperature programmed hydrogenation (TPH) and XPS measurement to C 1s are employed to elucidate the nature of coke on the spent catalysts. XPS spectra of C 1s for all spent catalysts are exhibited in Fig. 10 and Table S6. One broad shoulder (FWHM ∼ 1.1 eV) peak at 283.9 eV can be ascribed to the presence of adsorbed carbonaceous species strongly interacting with Ni surfaces [68,69]. It has also been observed that when Ni particles smaller than 10 nm interact with carbon, the C-Ni charge transfer will lead to a chemical shift towards lower binding energies, which normally lies within 0.3 eV [70]. The weak and broad peaks ranging from 288 to 291 eV originate from CO$_3^{2-}$ interacting strongly with basic MgO surfaces [71]. It is therefore concluded

that CO$_3^{2-}$ concentration on Mn$_{0.01}$-Ni$_{0.10}$Mg$_{0.90}$ is the highest (∼26 mol.%) among the spent catalysts, and most carbon species are either surface carbon or graphite type. H$_2$-TPH was also conducted to determine the types of carbon formed on the catalyst surfaces, as shown in Fig. 11 and Table 3. Two peaks can be distinguished to the pristine Ni$_{0.10}$Mg$_{0.90}$O, and the narrow peak (270–400 °C) centered at 318 °C can be attributed to C$_\alpha$, due to the presence of chemisorbed carbon atoms according to the assignment of McCarty and Trimm et al. [7,8]. On the other hand, Fujimoto et al. [72] also argue that the possibility of C$_\alpha$ due to the hydrogenation of adsorbed CO$_3^{2-}$ on the support surface cannot be ruled out in H$_2$-TPH. In this respect, C 1s XPS is complementary to the

Table 2
Surface composition and total coke content of spent catalysts.

Catalysts	Ni (mol.%)	Mg (mol.%)	C (mol.%)	M (promoter) (mol.%)	O	Coke[a] (wt.%)	Reaction rate[c] (mmol g^{-1} cat. s^{-1})
Ni$_{0.10}$Mg$_{0.90}$O	1.51	45.6	21.0		31.9	3.15	0.1170
Co$_{0.01}$-Ni$_{0.10}$Mg$_{0.90}$O	1.87	33.2	17.2	0.442	47.2	3.48	0.1235
Ce$_{0.01}$-Ni$_{0.10}$Mg$_{0.90}$O	0.875	36.5	19.6	0.355	42.7	4.04	0.1175
Sn$_{0.01}$-Ni$_{0.10}$Mg$_{0.90}$O	2.21	30.2	18.8	3.13	45.6	2.62	0.0139
Mn$_{0.01}$-Ni$_{0.10}$Mg$_{0.90}$O	1.53	25.6	24.2	Not found	48.7	24.03	0.0391
Ni$_{0.10}$Mg$_{0.90}$O[b]						26.65	0.0761
Co$_{0.01}$-Ni$_{0.10}$Mg$_{0.90}$O[b]						2.24	0.0710

[a] Measured by TG in air atmosphere.

[b] Tested under harsh reaction conditions (CH$_4$:CO$_2$ = 3:1, dilute gas free, 760 °C).

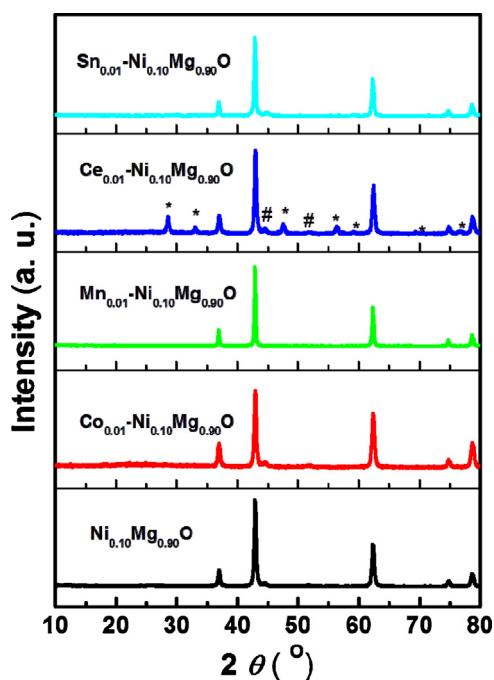[c] Derived from CH$_4$ initial conversion 760 °C.

Fig. 8. XRD patterns for the spent catalyst after 100 h catalytic test at 760 °C, # and * indicate diffractions from CeO_2 and Ni particles, respectively.

assignment, from which it is seen that only small amount (less than 15 mol.% except $Mn_{0.01}$-$Ni_{0.10}Mg_{0.90}O$) of CO_2 species can be identified. It is therefore confirmative that C_α is mainly from chemisorbed carbon atom that is reactive intermediate when CH_4 is progressively deprotonated, and can be gasified to CO during the course of reaction [18]. Furthermore, at the reaction
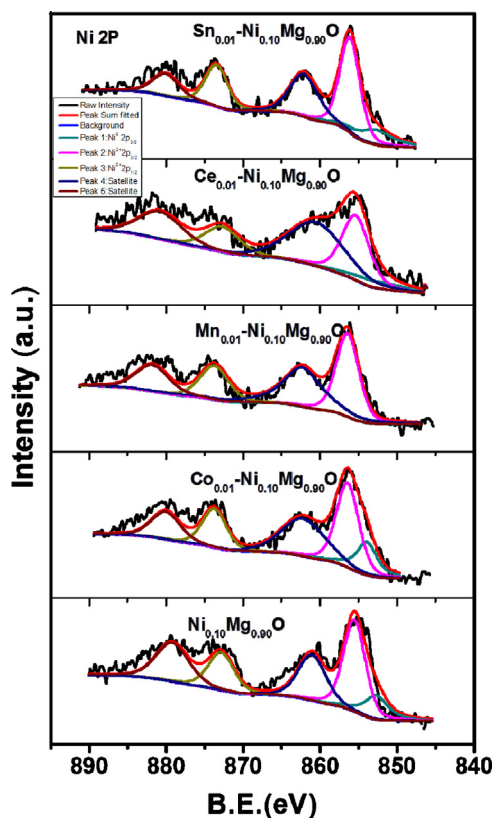

Fig. 10. C 1s XPS of the spent catalysts.

temperature of 760 °C, it is less likely to form thermally stable carbonate species at the catalyst surfaces, as CO_2 desorbs at lower temperatures [40,41]. It is thereby inferred that the small amount of CO_3^{2-} is from contamination of chemisorbed CO_2 when the spent catalysts are exposed to air. Besides, the other very broad peak

Fig. 9. XPS patterns of Ni 2P of the spent catalysts.

Fig. 11. H_2-TPH patterns of the spent catalysts.

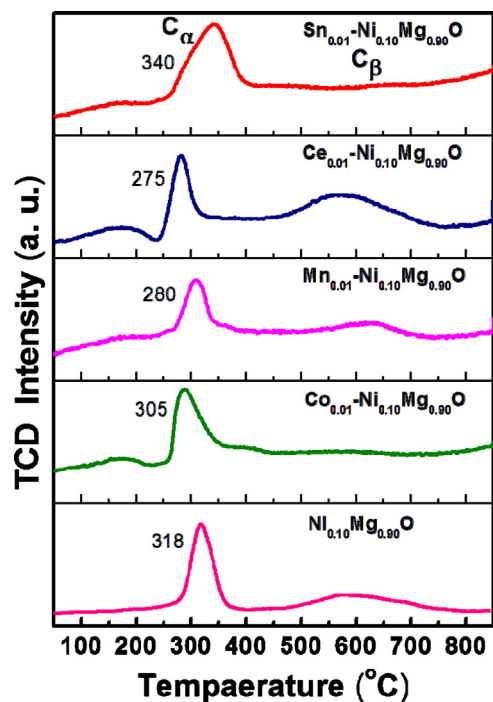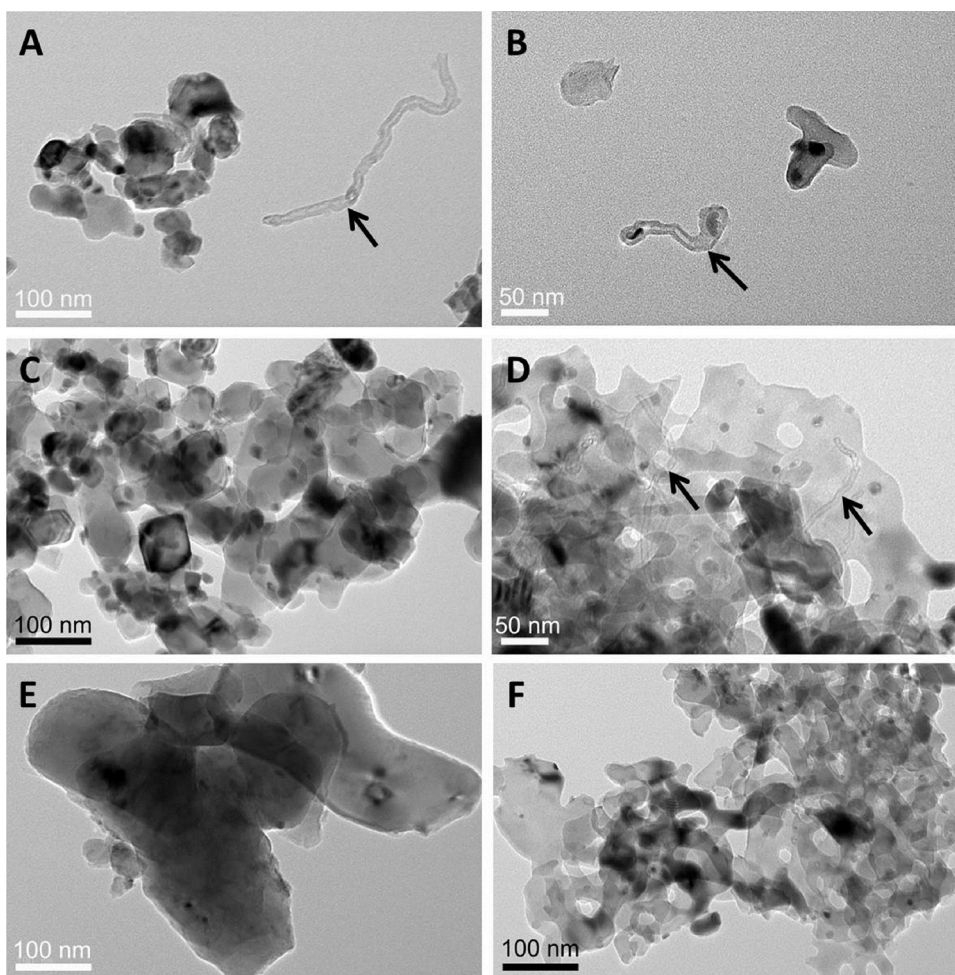**Fig. 12.** TEM images of spent catalysts, pristine $Ni_{0.10}Mg_{0.90}O$ (a, b), $Sn_{0.01}-Ni_{0.10}Mg_{0.90}O$ (c), $Ce_{0.01}-Ni_{0.10}Mg_{0.90}O$ (d), $Mn_{0.01}-Ni_{0.10}Mg_{0.90}O$ (e), and $Co_{0.01}-Ni_{0.10}Mg_{0.90}O$ (f). Whisker carbons are designated by arrows.

above 480 °C (480–750 °C) can be attributed to the hydrogenation of deposited carbon C_β, which is less reactive polymeric carbons on Ni surfaces, and can accumulate to form graphitic whisker carbon for prolonged time-on-stream test [7,8,18]. A more recalcitrant carbonaceous specie identified to hydrogenate at temperatures above 792 °C by Xu et al. [18] is not found in our measurement. It is also deduced that only on the pristine $Ni_{0.10}Mg_{0.90}O$, $Ce_{0.01}-Ni_{0.10}Mg_{0.90}O$ and $Mn_{0.01}-Ni_{0.10}Mg_{0.90}O$ can C_β be formed, whereas the C_β formation is virtually suppressed on $Co_{0.01}-Ni_{0.10}Mg_{0.90}O$ and $Sn_{0.01}-Ni_{0.10}Mg_{0.90}O$, as evidenced by the very low $C_\beta/(C_\alpha+C_\beta)$ ratios (Table 3). As a rule, C_α is initially formed on Ni surfaces as the only carbonaceous species, and can be an intermediate when CH_4 is deprotonated. C_β is seen after C_α accumulation on Ni surfaces for prolonged tests, as a result of high C_α concentration or slow gasification [7,18,72]. It is noteworthy that C_β has been found

unanimously in previously reported Ni-MgO solid solution catalysts during dry reforming, and this is the first observation that C_β formation is inhibited by promoters.

To further understand the effect of promoters on coke content and reactivity, we employed TG to measure the total carbon contents (Table 2). Low carbon contents were deduced, suggesting that the (1 1 1) $Ni_{0.10}Mg_{0.90}O$ platelet is a stable system against coke. The weight increase due to metal oxidation cannot be ruled out, and therefore the values can be underestimated (Table 2). TEM measurements to the spent catalysts are shown in Fig. 12, and the mean particle sizes of nickel are listed in Table 3 (calculated from Fig. S11). The metallic Ni^0 particle sizes are comparable for the spent catalysts with respect to the reduced ones, indicating that the particle size increases slightly after the tests. For the images for pristine $Ni_{0.10}Mg_{0.90}O$ catalyst are exhibited in Fig. 12a and b, from which whisker carbons can be found, albeit in small amount. It is also seen that whisker carbons can be found all over the spent $Ce_{0.01}-Ni_{0.10}Mg_{0.90}O$ catalyst, even more frequent than for pristine $Ni_{0.10}Mg_{0.90}O$. No whisker carbons are seen on spent $Co_{0.01}-Ni_{0.10}Mg_{0.90}O$, $Sn_{0.01}-Ni_{0.10}Mg_{0.90}O$ or $Mn_{0.01}-Ni_{0.10}Mg_{0.90}O$ catalysts. $Mn_{0.01}-Ni_{0.10}Mg_{0.90}O$ platelet is found to be agglomerated, whose size normally exceeds 100 nm and no nickel particles can be found. As the platelet size of $Mn_{0.01}-Ni_{0.10}Mg_{0.90}O$ is larger than in the case of the fresh sample (Fig. S7), we therefore infer that aggregation and dissolving of Mn^{2+} is incurred by the presence of MnO species on $Ni_{0.10}Mg_{0.90}O$. It is evident from XPS measurement that no Mn presents on the surface of spent $Mn_{0.01}-Ni_{0.10}Mg_{0.90}O$

Table 3
Coke determined by H_2-TPH measurement of robust systems and Ni particle size.

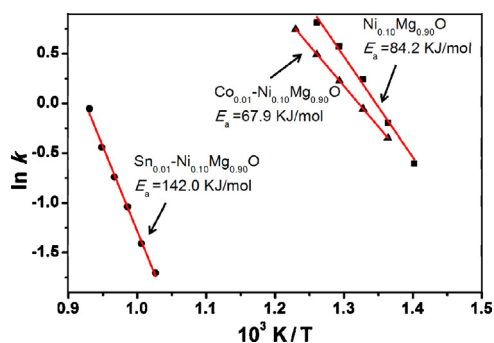| Sample	$C_\beta/(C_\alpha + C_\beta)$	Mean Ni Particle size (nm)[a]	
		As-reduced	Spent
$Ni_{0.10}Mg_{0.90}O$	37.82%	11	14
$Sn_{0.01}-Ni_{0.10}Mg_{0.90}O$	0.30%	15	16
$Ce_{0.01}-Ni_{0.10}Mg_{0.90}O$	52.82%	8	10
$Mn_{0.01}-Ni_{0.10}Mg_{0.90}O$	34.05%	Not detectable	
$Co_{0.01}-Ni_{0.10}Mg_{0.90}O$	0.70%	11	11

[a] Particle size of nickel obtained from TEM.

Fig. 13. Arrhenius plots of the CH₄ consumption rate obtained with the reactor operating under differential reaction conditions.

(Fig. S9), as Mn^{2+} may diffuse into the $Ni_{0.10}Mg_{0.90}O$ when Ni^0 comes out upon reduction. The platelet sizes of the other $M_{0.01}$-$Ni_{0.10}Mg_{0.90}O$ catalysts are almost identical to the as-calcined fresh catalysts, and hence it is conclusive that only $Co_{0.01}$-$Ni_{0.10}Mg_{0.90}O$ and $Sn_{0.01}$-$Ni_{0.10}Mg_{0.90}O$ are robust catalysts that over-perform the others in terms of coke-resistance or stability.

3.5. Kinetic studies of robust catalysts

To further understand the role of promoters in the stable catalysts, we undertake kinetic studies under differential reactor model, and the results are presented in Fig. 13. The activation energy measured for the pristine $Ni_{0.10}Mg_{0.90}O$ catalyst is 84.2 kJ/mol, a value that is lower than previously reported 105 kJ/mol [44], and we ascribe this discrepancy to the material difference. As our solid solution is orientated along [1 1 1] axis and the surface is of Tasker III type, it can be substantially different from randomly orientated particles. For $Co_{0.01}$-$Ni_{0.10}Mg_{0.90}O$ catalyst, the measurement gives activation energy of 67.9 kJ/mol, which is lower than that for pristine $Ni_{0.10}Mg_{0.90}O$. The $Sn_{0.01}$-$Ni_{0.10}Mg_{0.90}O$ catalyst, on the other hand, has rather high activation energy of 142.0 kJ/mol. The much higher activation energy implies that Sn covers the reactive sites on Ni surfaces, as suggested recently by Linic and co-workers for methane steam reforming reaction [33,62,73].

3.6. Catalytic performances of $Ni_{0.10}Mg_{0.90}O$ (1 1 1) and $Co_{0.01}$-$Ni_{0.10}Mg_{0.90}O$ (1 1 1) platelets under harsh reaction conditions

To evaluate the coke-resistance properties of $Co_{0.01}$-$Ni_{0.10}Mg_{0.90}O$ (1 1 1) platelet catalyst, a more critical CH_4: CO_2 feed ratio of 3:1 (total flow rate: 68 ml/min) is adopted to the speed up the coking process and exaggerate the difference, with the same space velocity (20,000 ml h⁻¹ g⁻¹ cat) and diluent gas free. Wang and Lu have proved that an increased methane concentration in methane dry reforming reaction will lead to substantial mass gain of coke [74]. $Co_{0.01}$-$Ni_{0.10}Mg_{0.90}O$ exhibits only a small enhancement in activity and stability with respect to pristine $Ni_{0.10}Mg_{0.90}O$ under normal time-on-stream tests (Fig. 7). It is observed that $Co_{0.01}$-$Ni_{0.10}Mg_{0.90}O$ is more robust under such harsh conditions than pristine $Ni_{0.10}Mg_{0.90}O$ catalyst (Fig. 14), with almost identical final activity as the initial activity. On the other hand, an obvious and deactivation is detected for pristine $Ni_{0.10}Mg_{0.90}O$ sample. TG is conducted to measure the coke contents for the two spent catalysts, only 2.24 wt.% is found on spent $Co_{0.01}$-$Ni_{0.10}Mg_{0.90}O$, whereas 26.65 wt.% is found on spent $Ni_{0.10}Mg_{0.90}O$ catalyst (Table 2). For $Co_{0.01}$-$Ni_{0.10}Mg_{0.90}O$, the coke content is close to that under normal conditions (Fig. S12 and Table 2). But for pristine $Ni_{0.10}Mg_{0.90}O$, the coke content is increased from 3.15 wt.% to 26.65 wt.%. From this observation, it is inferred that coke

deposition causes deactivation under harsh reaction conditions. Co- promotes long term stability for $Ni_{0.10}Mg_{0.90}O$ in our system.

3.7. Discussion

We have shown that Sn, Ce, Mn and Co can be incorporated into $Ni_{0.10}Mg_{0.90}(OH)(OCH_3)$ to generate promoted $M_{0.01}$-$Ni_{0.10}Mg_{0.90}O$ (1 1 1) platelet. The structural evolution and promoting effect are discussed separately in the following part. To understand the interplay between catalyst structure and coke deposition, it is important to take into consideration the kinetics and mechanism. Iglesia and Wei [44] have shown that the reaction rate for $Ni_xMg_{1−x}O$ is controlled by CH_4 fragmentation (elementary reaction (7)), $r = kP_{CH_4}$, which is also in consistent with theoretical estimation by Nørskov et al. [6]. The progressive deprotonation of CH_4 can lead to the formation of C_α that is an intermediate (elementary reaction (8)). High surface coverage of C_α will lead its polymerization into recalcitrant C_β (elementary reaction (9)). The gasification of as-formed coke species is mainly due to the thermodynamically feasible reverse Boudouard reaction (elementary reaction (10)) under the reacting conditions. C_β is prone to nucleate and grow on Ni surfaces that result in whisker carbon growth (reaction (11)), for which the step sites are required [6,9]. At temperatures for dry reforming, the surface is clean as a result of low adsorption energy for most intermediates involved [10,75]. The (1 1 1) surface of $Ni_xMg_{1−x}O$ is made up of alternating positively charged Mg^{2+} layers and negatively charged $O^{2−}$ layers, and the lattice [*O] can participate in the gasification of carbonaceous species via spillover to Ni surfaces [15,21]. In addition, the Tasker III surface interacts strongly with metallic Ni can assist to stable the as-reduced Ni particles. Ni surfaces are covered by various sites, among which the under coordinated ones such as steps or kinks possess a lower activation energy, whereas terraces have a relatively higher activation energy. As coke formation is initiated at the under coordinated sites, blockage of such centers is essential for the design of coke-resistant catalyst, which is accompanied by the passivation of Ni surfaces. A non-passivation Ni catalyst would need to enhance the gasification step to achieve stability. The roles of these promoters and their performances are discussed separately in the following by taking into consideration the above mechanism.

Mn^{2+} presents in the solid solution, but does not alloy with Ni for the zero anti-segregation energy and resistance to be reduced to metallic Mn^0 [59,65]. Mn^{2+} has a strong affinity and close ionic radius to Mg^{2+}, and there is a driving force to separate from Ni^0 surface and dissolve into $Ni_{0.10}Mg_{0.90}O$ in the long term test at high temperature. As a result, no surface Mn species was found on the spent $Mn_{0.01}$-$Ni_{0.10}Mg_{0.90}O$ catalyst. Mn^{2+} dissolved into the solid solution may still have strong interaction with Ni, which leads to inhibition of Ni^0 growth and therefore no large particle was found for the fresh and spent catalyst by XRD. The very small Ni^0 particles can help to inhibit the nucleation of whisker carbon, but not the formation of C_β, and H_2-TPH results advocate such speculations. It is thereby inferred that Mn inhibits reduction of Ni^{2+} in the initial stage of reduction or reaction. In the long run, Mn^{2+} diffuses into the bulk but retains a strong interaction with surface Ni^0, and stops the surface diffusion and further growth of Ni particulates. At the same time, MnO species also accelerate the fusion of $Ni_{0.10}Mg_{0.90}O$ particles at high temperatures, which decreases the overall surface area and results in quick catalyst deactivation.

Sn^{4+}/Sn^{2+} can be reduced in the H_2 pretreatment to Sn^0. Sn^0 has been observed and predicted to exist on Ni surfaces as adatoms via forming surface alloys, which is capable of inhibiting coke deposition in steam reforming of methane as proposed by Linic et al. [33,62,73]. Substantial enrichment of Sn is therefore found on the surface of $Sn_{0.01}$-$Ni_{0.10}Mg_{0.90}O$, because Sn forms surface alloy with
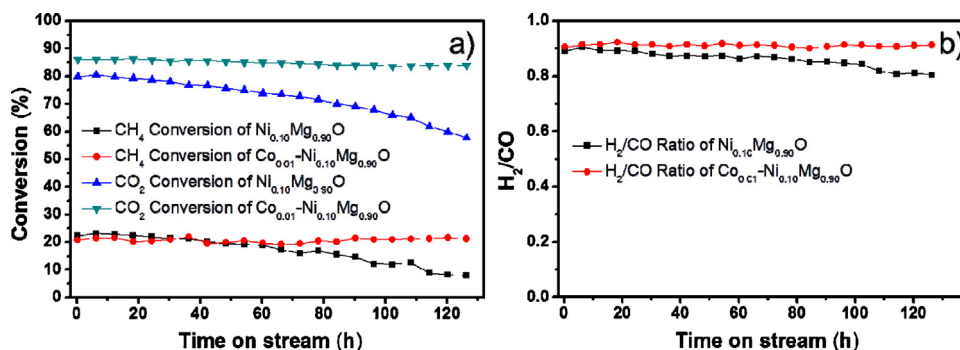
Fig. 14. Time-on-stream (a and b) dependent CH_4-CO_2 dry reforming performance for pristine and $Co_{0.01}$-$Ni_{0.10}Mg_{0.90}O$, and time-on-stream stabilities in the 125 h test under harsh reaction conditions at 760 °C.

Ni as a result of strong thermodynamic driving force. As Sn prefers to bind on under coordinated Ni surface step sites, which are kinetically more reactive for reforming of methane and susceptible to coke deposition. It is inferred that Sn blocks these reactive sites via "ensemble control" of active site, and hence mitigates the coking of Ni surfaces. This deduction is in line with the elevation of activation energies, suggesting the role of Sn in dry reforming is similar to that of steam reforming. From H_2-TPR measurement, it is also known that Sn enhances the catalyst affinity to oxygen, which is important to gasification of surface carbonaceous species. Sn-Ni surface alloy is also estimated to bind more strongly to oxygen species rather than carbon species, which is believed to favor coke gasification and disfavor coke deposition [62]. Resultantly, negligible amount of C_β is found in spent $Sn_{0.01}$-$Ni_{0.10}Mg_{0.90}O$ catalyst. The increase in activity suggests that more Ni is reduced during long term tests, indicating that the solid solution undergoes continuous reduction during test as a result of affinity towards oxygen during H_2 pretreatment. The XRD measurement also indicate the incomplete reduction of Sn^{2+} in the as-reduced sample and its absence in the spent sample, this may cause the fluctuation in catalytic time-on-stream test.

CeO_2 is known to be a reducible metal oxide that can promote the reducibility of $Ni_{0.10}Mg_{0.90}O$ support on one hand, and is supposed to promote the coke-resistance dynamically by the oxygen storage/release capacity that is important to the gasification of carbonaceous species. From our tests, however, Ce- additive has no obvious impact on coke formation and a large number of whisker carbons are found in spent $Ce_{0.01}$-$Ni_{0.10}Mg_{0.90}O$. NiO has a limited solubility (10–12 mol.%) in CeO_2 but unlimited solubility in MgO [76], that is why the fresh $Ce_{0.01}$-$Ni_{0.10}Mg_{0.90}O$ catalyst is made up of $Ni_{0.10}Mg_{0.90}O$ solid solution and isolated CeO_2. Theoretical predications also suggest that vacancies on CeO_2 surfaces are metallic in nature [77], and *in situ* studies shows that CeO_2 will migrate to Ni surfaces under reducing atmosphere [78]. Under the reducing reacting atmosphere, more vacancies are formed, making CeO_2 surface more wettable to metallic Ni^0, which actually accelerates the growth of metallic Ni particles. The growth can lead to the formation of larger Ni^0 particles that are known to be susceptible to coke-deposition, and is hence detrimental to the coke-resistant performance. These findings clearly show that under reducing atmosphere the oxygen storage/release capacity of CeO_2 is limited and the interface is unstable.

Co has a high affinity towards surface oxygen species (O or OH) [10,79,80], and these intermediate species formed during catalytic reaction can attract Co on the alloy surfaces. Co seems to possess coke-resistant properties as a result of its affinity towards oxygen species, which guarantees a high surface coverage of O or OH that is important to the gasification of deposited carbon. But pristine Co based catalysts are susceptible towards oxidation or oxygen caused poisoning [79,80], and a balanced Co-Ni ratio on the surface is

essential to the coke- or oxygen-induced deactivation. According to our experimental results (Fig. 14), we can conclude that a Co- addition enhances the stability against coke formation. Ni and Co alloys with a moderate anti-segregation energy (0.13 eV) that ensures homogeneous mixing of the two metals during the course of the reaction [65]. This is the reason why the spent catalyst has similar cobalt content to that of the fresh sample. In the dry reforming reaction pathway, methane fragmentation is the rate determining step and the effect of Co on gasification is kinetically favorable, as activation energy is lowered. Theoretical studies suggest that CH_4 prefers to activate on Co sites of Co-Ni alloy, resulting in lowered activation energy [66]. H_2-TPR shows that Co elevates the reduction temperature of $Co_{0.01}$-$Ni_{0.10}Mg_{0.90}O$ with respect to pristine $Ni_{0.10}Mg_{0.90}O$, implying the Co-Ni alloy has a stronger affinity towards oxygen species. We therefore attribute the coke-resistant stability of $Co_{0.01}$-$Ni_{0.10}Mg_{0.90}O$ catalyst to the enhanced gasification of intermediate C_α by oxygen species. The timely gasification also suggests a low surface coverage and less likely polymerization towards C_β formation, which is not found by H_2-TPH measurement to the spent $Co_{0.01}$-$Ni_{0.10}Mg_{0.90}O$ catalyst.

Despite the fact that $Ni_xMg_{1-x}O$ is a robust catalyst for dry reforming for the ultrafine Ni particle size after reduction, the unpromoted Ni surfaces still possess both terraces and under coordinated sites. The presence of C_β and whisker carbon is a result of exposed steps that facilitate coke nucleation and growth. Although promoting effect has been previously reported, the distribution of metals is not controlled. Consequently, the relationship between catalysis and structure is based on microscopically mixed species that exhibit various active sites. In the present work, zoning of Ce and Mn are found during catalyst preparation and lack of promoters actually causes coke deposition. But the result does not suggest that Ce or Mn is not a promoter, since they may behave as spectators in catalysis. On the other hand, Co or Sn is shown to be uniformly distributed and henceforth guarantees the coke-free run all through the catalysts. In this respect, these results give a clear relationship between micro-structure and macro-catalysis.

4. Conclusions

We demonstrate that $M_{0.01}$-$Ni_{0.10}Mg_{0.90}(OH)(OCH_3)$ is precursor for the synthesis of promoted $Ni_{0.10}Mg_{0.90}O$ catalyst, as the surface orientation is controlled to (1 1 1) facets for $Ni_{0.10}Mg_{0.90}O$ solid solution. The structural evolution in preparation and catalytic performances in CH_4-CO_2 dry reforming are explored. Ce- segregates as CeO_2 because it is immiscible with MgO. Mn- forms MnO species of amorphous nature, which actually causes agglomeration of $Ni_{0.10}Mg_{0.90}O$ particles under reforming conditions. Addition of Co or Sn produces solid solution with homogeneous elemental distribution after thermal decomposition of the precursor. It is

found that only Co and Sn inhibit the formation of C_β, whereas Mn or Ce has no obvious suppressing effect towards C_β. Only on pristine and Ce-promoted $Ni_{0.10}Mg_{0.90}O$ can whisker carbons form, despite that C_β is also formed on $Mn_{0.01}$-$Ni_{0.10}Mg_{0.90}O$. $Mn_{0.01}$-$Ni_{0.10}Mg_{0.90}O$ suffers from severe sintering of primary particle in long term catalytic run. Mn inhibits Ni^0 growth in both reduction and 100 h time-on-stream test, but does not suppress the formation of C_β. Both $Sn_{0.01}$-$Ni_{0.10}Mg_{0.90}O$ and $Co_{0.01}$-$Ni_{0.10}Mg_{0.90}O$ are found to be durable catalyst for CH_4-CO_2 reforming, but the roles of Sn and Co are different. Sn is found to be enriched on catalyst surfaces and an increase in activation energy is observed for $Sn_{0.01}$-$Ni_{0.10}Mg_{0.90}O$, strongly suggesting it reconstructs to form surface alloy with Ni^0. The surface concentration of Co is close to that in the bulk $Co_{0.01}$-$Ni_{0.10}Mg_{0.90}O$, and does not passivate the pristine $Ni_{0.10}Mg_{0.90}O$ catalyst. We conclude that $Co_{0.01}$-$Ni_{0.10}Mg_{0.90}O$ derived from our solvothermal method is a non-passivated catalyst for CH_4-CO_2 dry reforming as a result of evenly distribution of both metals. The fact that only well dispersed promoters can inhibit the formation of C_β suggests that distribution of promoters are crucial to the enhancement of catalyst stability. Further explorations of the effect of feedstock and Co/Ni ratios on catalytic performances for the system are currently undertaken and will be reported in the future.

Supporting information

SEM, TEM, TG and IR characterizations of the intermediate $M_{0.01}$-$Ni_{0.10}Mg_{0.90}(OH)(OCH_3)$, TEM and elemental mapping information of $M_{0.01}$-$Ni_{0.10}Mg_{0.90}O$, details of XPS measurements are shown in the Supporting Information. This material is available free of charge via Internet at http://www.sciencedirect.com/.

Acknowledgments

Appendix A. Supplementary data

Supplementary data associated with this article can be found, in the online version, at http://dx.doi.org/10.1016/j.apcatb.2013.10.046.

References

[1] J.R. Rostrup-Nielsen, J. Sehested, J.K. Nørskov, in: H.K. Bruce Gates (Ed.), Advances in Catalysis, 2nd ed., Academic Press, New York, 2002, pp. 65–139.
[2] J.P. Van Hook, Catal. Rev. Sci. Eng. 21 (1980) 1–51.
[3] C.-j. Liu, J. Ye, J. Jiang, Y. Pan, ChemCatChem 3 (2011) 529–541.
[4] S. Helveg, J. Sehested, J.R. Rostrup-Nielsen, Catal. Today 178 (2011) 42–46.
[5] J.G. Zhang, H. Wang, A.K. Dalai, J. Catal. 249 (2007) 300–310.
[6] H.S. Bengaard, J.K. Nørskov, J. Sehested, B.S. Clausen, L.P. Nielsen, A.M. Molenbroek, J.R. Rostrup-Nielsen, J. Catal. 209 (2002) 365–384.
[7] J.G. McCarty, H. Wise, J. Catal. 57 (1979) 406–416.
[8] D.L. Trimm, Catal. Today 49 (1999) 3–10.
[9] S. Helveg, C. Lopez-Cartes, J. Sehested, P.L. Hansen, B.S. Clausen, J.R. Rostrup-Nielsen, F. Abild-Pedersen, J.K. Nørskov, Nature 427 (2004) 426–429.
[10] G. Jones, J.G. Jakobsen, S.S. Shim, J. Kleis, M.P. Andersson, J. Rossmeisl, F. Abild-Pedersen, T. Bligaard, S. Helveg, B. Hinnemann, J.R. Rostrup-Nielsen, I. Chorkendorff, J. Sehested, J.K. Nørskov, J. Catal. 259 (2008) 147–160.
[11] S. Gaur, D.J. Haynes, J.J. Spivey, Appl. Catal. A: Gen. 403 (2011) 142–151.
[12] S.M. Lima, J.M. Assaf, M.A. Peña, J.L.G. Fierro, Appl. Catal. A: Gen. 311 (2006) 94–104.
[13] Y.H. Hu, Catal. Today 148 (2009) 206–211.
[14] Y.H. Hu, E. Ruckenstein, Catal. Rev. Sci. Eng. 44 (2002) 423–453.
[15] E. Ruckenstein, Y. Hu, Catal. Lett. 51 (1998) 183–185.
[16] E. Ruckenstein, Y.H. Hu, Appl. Catal. A: Gen. 133 (1995) 149–161.
[17] Y.-H. Wang, H.-M. Liu, B.-Q. Xu, J. Mol. Catal. A: Chem. 299 (2009) 44–52.
[18] Y.-H. Wang, H. Wang, Y. Li, Q.-M. Zhu, B.-Q. Xu, Top. Catal. 32 (2005) 109–116.
[19] T. Horiuchi, K. Sakuma, T. Fukui, Y. Kubo, T. Osaki, T. Mori, Appl. Catal. A: Gen. 144 (1996) 111–120.
[20] E. Ruckenstein, Y. Hu, Appl. Catal. A: Gen. 154 (1997) 185–205.
[21] K. Tomishige, O. Yamazaki, Y. Chen, K. Yokoyama, X. Li, K. Fujimoto, Catal. Today 45 (1998) 35–39.
[22] Y.-g. Chen, K. Tomishige, K. Yokoyama, K. Fujimoto, Appl. Catal. A: Gen. 165 (1997) 335–347.
[23] A. Djaidja, S. Libs, A. Kiennemann, A. Barama, Catal. Today 113 (2006) 194–200.
[24] M. Nurunnabi, B. Li, K. Kunimori, K. Suzuki, K.-i. Fujimoto, K. Tomishige, Appl. Catal. A: Gen. 292 (2005) 272–280.
[25] M. Nurunnabi, Y. Mukainakano, S. Kado, B. Li, K. Kunimori, K. Suzuki, K.-i. Fujimoto, K. Tomishige, Appl. Catal. A: Gen. 299 (2006) 145–156.
[26] A.E. Castro Luna, M.E. Iriarte, Appl. Catal. A: Gen. 343 (2008) 10–15.
[27] G.A. Olah, A. Goeppert, M. Czaun, G.K. Prakash, J. Am. Chem. Soc. 135 (2013) 648–650.
[28] Y.H. Hu, E. Ruckenstein, Catal. Lett. 36 (1996) 145–149.
[29] Y.H. Hu, E. Ruckenstein, Catal. Lett. 43 (1997) 71–77.
[30] O. Yamazaki, K. Tomishige, K. Fujimoto, Appl. Catal. A: Gen. 136 (1996) 49–56.
[31] B.Q. Xu, J.M. Wei, H.Y. Wang, K.Q. Sun, Q.M. Zhu, Catal. Today 68 (2001) 217–225.
[32] K. Tomishige, Y. Himeno, Y. Matsuo, Y. Yoshinaga, K. Fujimoto, Ind. Eng. Chem. Res. 39 (2000) 1891–1897.
[33] E. Nikolla, J. Schwank, S. Linic, J. Catal. 250 (2007) 85–93.
[34] F. Besenbacher, I. Chorkendorff, B.S. Clausen, B. Hammer, A.M. Molenbroek, J.K. Nørskov, I. Stensgaard, Science 279 (1998) 1913–1915.
[35] V.M. Gonzalez-Delacruz, R. Pereniguez, F. Temero, J.P. Holgado, A. Caballero, ACS Catal. 1 (2011) 82–88.
[36] J.R. Rostrup-Nielsen, Chem. Eng. Sci. 50 (1995) 4061–4071.
[37] L. Espinosa-Alonso, M. O'Brien, S. Jacques, A. Beale, K. de Jong, P. Barnes, B. Weckhuysen, J. Am. Chem. Soc. 131 (2009) 16932–16938.
[38] K.K. Zhu, W.M. Hua, X.Y. Wang, Chem. Lett. 40 (2011) 156–158.
[39] J.C. Hu, K.K. Zhu, L.F. Chen, H.J. Yang, Z. Li, A. Suchopar, R. Richards, Adv. Mater. 20 (2008) 267.
[40] K.K. Zhu, J.C. Hu, C. Kubel, R. Richards, Angew. Chem. Int. Ed. 45 (2006) 7277–7281.
[41] K.K. Zhu, W. Hua, W. Deng, R.M. Richards, Eur. J. Inorg. Chem (2012) 2869–2876.
[42] H. Xiao, Z. Liu, X. Zhou, K. Zhu, Catal. Commun. 34 (2013) 11–15.
[43] P.W. Tasker, J.C. Phys, Solid State Phys. 12 (1979) 4977–4984.
[44] J. Wei, E. Iglesia, J. Catal. 224 (2004) 370–383.
[45] T. Kubo, K. Uchida, K. Tsubosaki, F. Hashimi, Kogyo Kagaku Zasshi 73 (1970) 75–82.
[46] S. Le Bihan, J. Guenot, M. Figlarz, J. Phys. Chem. Solids 17 (1976) 15–25.
[47] N. Bochvar, O. Fabrichnaya, Y. Liberov, in: G. Effenberg, S. Ilyenko (Eds.), Non-Ferrous Metal Ternary Systems. Selected Nuclear Materials and Engineering Systems: Phase Diagrams, Crystallographic and Thermodynamic Data, Springer, Heidelberg/Berlin, 2007, pp. 230–236.
[48] A.-M. Azad, L. Jing Min, Ceram. Int. 27 (2001) 325–334.
[49] R. Kannan, M.S. Seehra, Phys. Rev. B 35 (1987) 6847–6853.
[50] A.F. Carley, S.D. Jackson, J.N. O'Shea, M.W. Roberts, Phys. Chem. Chem. Phys. 3 (2001) 274–281.
[51] D. Alders, F.C. Voogt, T. Hibma, G.A. Sawatzky, Phys. Rev. B 54 (1996) 7716–7719.
[52] M. Oku, K. Hirokawa, J. Electron Spectrosc. Rel. Phenom. 10 (1977) 103–110.
[53] M.A. Stranick, A. Moskwa, Surf. Sci. Spectra 2 (1993) 45–49.
[54] H.F. Franzen, M.X. Umaña, J.R. McCreary, R.J. Thorn, J. Solid State Chem. 18 (1976) 363–368.
[55] D. Gazzoli, M. Occhiuzzi, A. Cimino, D. Cordischi, G. Minelli, F. Pinzari, J. Chem. Soc. Faraday Trans. 92 (1996) 4567–4574.
[56] A. Parmaliana, F. Arena, F. Frusteri, N. Giordano, J. Chem. Soc. Faraday Trans. 86 (1990) 2663–2669.
[57] G.C. Bond, S.P. Sarsam, Appl. Catal. 38 (1988) 365–377.
[58] H.Y. Wang, E. Ruckenstein, Appl. Catal. A: Gen. 209 (2001) 207–215.
[59] F. Kapteijn, L. Singoredjo, A. Andreini, J.A. Moulijn, Appl. Catal. B: Environ. 3 (1994) 173–189.
[60] K. Zhou, X. Wang, X. Sun, Q. Peng, Y. Li, J. Catal. 229 (2005) 206–212.
[61] J.-S. Choi, K.-I. Moon, Y. Kim, J. Lee, C.-H. Kim, D. Trimm, Catal. Lett. 52 (1998) 43–47.
[62] E. Nikolla, J. Schwank, S. Linic, J. Am. Chem. Soc. 131 (2009) 2747–2754.
[63] J. Kehres, J.G. Jakobsen, J.W. Andreasen, J.B. Wagner, H. Liu, A. Molenbroek, J. Sehested, I. Chorkendorff, T. Vegge, J. Phys. Chem. C 116 (2012) 21407–21415.
[64] R.T. Vang, K. Honkala, S. Dahl, E.K. Vestergaard, J. Schnadt, E. Laegsgaard, B.S. Clausen, J.K. Nørskov, F. Besenbacher, Nat. Mater. 4 (2005) 160–162.
[65] A.V. Ruban, H.L. Skriver, J.K. Nørskov, Phys. Rev. B 59 (1999) 15990–16000.
[66] H. Liu, R. Zhang, R. Yan, B. Wang, K. Xie, Appl. Surf. Sci. 257 (2011) 8955–8964.
[67] L. Guczi, G. Stefler, O. Geszti, I. Sajó, Z. Pászti, A. Tompos, Z. Schay, Appl. Catal. A: Gen. 375 (2010) 236–246.
[68] S. Sinharoy, L.L. Levenson, Thin Solid Films 53 (1978) 31–36.
[69] P.M. Blass, S. Akhter, C.M. Seymour, J.J. Lagowski, J.M. White, Surf. Sci. 217 (1989) 85–102.
[70] C. Bittencourt, A. Felten, J. Ghijsen, J.J. Pireaux, W. Drube, R. Erni, G. Van Tendeloo, Chem. Phys. Lett. 436 (2007) 368–372.
[71] H. Onishi, C. Egawa, T. Aruga, Y. Iwasawa, Surf. Sci. 191 (1987) 479–491.
[72] K. Tomishige, Y.-g. Chen, K. Fujimoto, J. Catal. 181 (1999) 91–103.

[73] E. Nikolla, A. Holewinski, J. Schwank, S. Linic, J. Am. Chem. Soc. 128 (2006) 11354–11355.
[74] S. Wang, G.Q. Lu, Energy Fuels 12 (1998) 1235–1240.
[75] Y. Xu, C. Fan, Y.-A. Zhu, P. Li, X.-G. Zhou, D. Chen, W.-K. Yuan, Catal. Today 186 (2012) 54–62.
[76] L. Barrio, A. Kubacka, G. Zhou, M. Estrella, A. Martiínez-Arias, J.C. Hanson, M. Fernández-Garciía, J.A. Rodriguez, J. Phys. Chem. C 114 (2010) 12689–12697.
[77] S. Fabris, G. Vicario, G. Balducci, S. de Gironcoli, S. Baroni, J. Phys. Chem. B 109 (2005) 22860–22867.
[78] A. Caballero, J.P. Holgado, V.M. Gonzalez-delaCruz, S.E. Habas, T. Herranz, M. Salmeron, Chem. Commun. 46 (2010) 1097–1099.
[79] E. Ruckenstein, H.Y. Wang, J. Catal. 205 (2002) 289–293.
[80] K. Nagaoka, K. Takanabe, K.-i. Aika, Appl. Catal. A: Gen. 268 (2004) 151–158.